# Broadening of the I²P₁/₂>P₃/₂ Transition Lineshape by Unsteady Vortex Motion "Journal Article (Postprint)"

**Timothy J. Madden**

**21 August 2008**

**Interim Report**

**AIR FORCE RESEARCH LABORATORY**
**Directed Energy Directorate**
**3550 Aberdeen Ave SE**
**AIR FORCE MATERIEL COMMAND**
**KIRTLAND AIR FORCE BASE, NM 87117-5776**

# REPORT DOCUMENTATION PAGE

| 1. REPORT DATE *(DD-MM-YYYY)* | 2. REPORT TYPE | 3. DATES COVERED *(From - To)* |
|---|---|---|
| 21-08-2008 | Interim Report | 12-11-2004 to 21-08-2008 |

| 4. TITLE AND SUBTITLE | 5a. CONTRACT NUMBER |
|---|---|
| Broadening of the $I^2P_{1/2} \rightarrow {}^2P_{3/2}$ Transition Lineshape by Unsteady Vortex Motion Journal Article (Postprint) | In House (DF297846) |

5b. GRANT NUMBER

5c. PROGRAM ELEMENT NUMBER
62605F

| 6. AUTHOR(S) | 5d. PROJECT NUMBER |
|---|---|
| | 4866 |

5e. TASK NUMBER
LB

Timothy J. Madden

5f. WORK UNIT NUMBER
41

| 7. PERFORMING ORGANIZATION NAME(S) AND ADDRESS(ES) | 8. PERFORMING ORGANIZATION REPORT NUMBER |
|---|---|
| Air Force Research Laboratory<br>3550 Aberdeen Ave SE<br>Kirtland AFB, NM 87117-5776 | |

| 9. SPONSORING / MONITORING AGENCY NAME(S) AND ADDRESS(ES) | 10. SPONSOR/MONITOR'S ACRONYM(S) |
|---|---|
| Air Force Research Laboratory<br>3550 Aberdeen Ave SE<br>Kirtland AFB, NM 87117-5776 | |
| | 11. SPONSOR/MONITOR'S REPORT NUMBER(S)<br>AFRL-RD-PS-TP-2008-1012 |

**12. DISTRIBUTION / AVAILABILITY STATEMENT**

Approved for public release; distribution is unlimited.

**13. SUPPLEMENTARY NOTES**
Published in the Proceedings of the 39th American Institute of Aeronautics and Astronautics Plasmadynamics and Lasers Conference, 22-26 June, 2008, Seattle, WA.

**14. ABSTRACT**
   The spectroscopically measured lineshape of an atomic transition provides a wealth of useful information relative to diagnosing The use of atomic transition lineshapes to ascertain the temperature of a gas stems to the 1920s, particularly within the astronomical community. Indeed, this community was the first to recognize the potential contribution of large scale bulk motion of the gas to the breadth of the spectroscopic measurement of transition lineshapes beyond that of the random molecular motion associated with temperature. In 1934 Stuve and Elvey showed that by including a bulk gas velocity Doppler broadening term in the Voigt equation for the transition lineshape in addition to the random thermal motion term, it was possible to estimate whether a stellar atmosphere was 'turbulent' or not based upon the fit of the Voigt equation to the measured transition lineshapes for that atmosphere. Taking the theory a step further, using estimated optical paths or length scales for the stellar atmospheres that they were measuring, they were able to estimate median gas velocities and correlate increasing velocity magnitude with increasing temperature of the stellar atmosphere based upon the Voigt fit.

**15. SUBJECT TERMS**
Lineshape, COIL, flow, doppler

| 16. SECURITY CLASSIFICATION OF: | | | 17. LIMITATION OF ABSTRACT | 18. NUMBER OF PAGES | 19a. NAME OF RESPONSIBLE PERSON<br>Timothy J. Madden |
|---|---|---|---|---|---|
| **a. REPORT**<br>UNCLASSIFIED | **b. ABSTRACT**<br>UNCLASSIFIED | **c. THIS PAGE**<br>UNCLASSIFIED | UNLIMITED | 20 | **19b. TELEPHONE NUMBER** *(include area code)*<br>505-846-9076 |

# Broadening of the I $^2P_{1/2} \rightarrow {}^2P_{3/2}$ Transition Lineshape by Unsteady Vortex Motion

Timothy J. Madden[1]
*US Air Force Research Laboratory, Directed Energy Directorate*
*Kirtland AFB, NM 87117-5776*

**Introduction.**
  The spectroscopically measured lineshape of an atomic transition provides a wealth of useful information relative to diagnosing The use of atomic transition lineshapes to ascertain the temperature of a gas stems to the 1920s, particularly within the astronomical community.  Indeed, this community was the first to recognize the potential contribution of large scale bulk motion of the gas to the breadth of the spectroscopic measurement of transition lineshapes beyond that of the random molecular motion associated with temperature.  In 1934 Stuve and Elvey[1] showed that by including a bulk gas velocity Doppler broadening term in the Voigt equation for the transition lineshape in addition to the random thermal motion term, it was possible to estimate whether a stellar atmosphere was 'turbulent' or not based upon the fit of the Voigt equation to the measured transition lineshapes for that atmosphere.   Taking the theory a step further, using estimated optical paths or length scales for the stellar atmospheres that they were measuring, they were able to estimate median gas velocities and correlate increasing velocity magnitude with increasing temperature of the stellar atmosphere based upon the Voigt fit.

  More recently, continuously tunable diode lasers have been applied to lineshape measurement of transitions within species in the COIL flowfield as a means to determine number density of those species as well as laser gain on the I $^2P_{1/2} \rightarrow {}^2P_{3/2}$ transition.  Davis and Allen et al[2,3,4,5] applied lineshape measurement and Voigt fitting methods to various COIL species as a mechanism to determine concentration and translational temperature in the COIL flowfield as an experiment diagnostic.  While the effect of the bulk gas velocity was not taken into account in these investigations, the diagnostics developed by these investigations provided the means to do so.  Nikolaev et al,[6] applied the same type of continuously tunable diode laser to the I $^2P_{1/2} \rightarrow {}^2P_{3/2}$ transition to investigate the influence of mean gas velocity through a COIL device upon the laser gain.  They showed that by varying the angle at which the diode laser beam passes through the COIL flowfield, the line center gain can be varied.  Using this mechanism, they were able to determine the mean flow velocity for the COIL and convert the laser gain diagnostic into a flow diagnostic.  Similarly, they recognized the propensity for 'turbulence' to contribute to the broadening of the lineshape.  Invoking statistical turbulence theory, they suggested a 10 K influence of the velocity components associated with the vertical structures modeled by this theory upon the temperatures extracted from the lineshapes measured on their COIL device.  The issue of flow unsteadiness as examined here relates directly to this work by Nikolaev et al as the velocity components associated with the unsteady eddies generated by jet-in-crossflow interaction between the He/I$_2$ secondary flow with the He/O$_2$($^1\Delta$) primary flow are directly simulated counterparts to those modeled in the statistical turbulence theory.  In this light, this work may shed some light on the applicability of turbulence models to the low Reynolds number COIL flowfields.

  The lineshape of the I $^2P_{1/2} \rightarrow {}^2P_{3/2}$ transition provides a means to ascertain a variety of useful information regarding the performance of the chemical oxygen-iodine laser (COIL).  The value at the center of the lineshape, commonly referred to as the 'line center,' is proportional to the laser amplification on the I $^2P_{1/2} \rightarrow {}^2P_{3/2}$ transition.  The infinite integral of the lineshape is proportional to the number density of the ground and excited states of atomic iodine in the gas, indicating the degree of I$_2$ dissociation.  And the width of the lineshape indicates the amount of broadening of the transition, both due to collisional and Doppler shift effects.  As the Doppler shift is proportional to velocity, the width of the transition can be used to estimate the degree of random molecular motion in the gas, expressed in macroscopic terms as temperature.  A Doppler shift to the frequencies in the transition can also occur through the straight-line, bulk motion of the gas, and this can be used to examine the velocity field of the gas.  However, the flow may experience rotation through the presence of eddies carried within the gas, and these too may contribute to the Doppler shift of the lineshape frequencies.  Given that eddies by virtue of their positive and negative velocity components can induce positive and negative Doppler shift, the widening of the lineshape is similar to thermal motion which also includes positive and

---

[1] Senior Member, AIAA.

negative velocities. Thus, when interpreting transition lineshapes, if some account is not made for both thermal and rotational motion, the effect of either physical process will be over-estimated.

The work discussed here is oriented toward examining the interplay between the gas dynamics and the lineshape of the I $^2P_{1/2} \rightarrow ^2P_{3/2}$ transition, and in turn determine the ramifications for the use of spectroscopic lineshape based diagnostics and interpretation of their data. These efforts in turn are directly linked to efforts improve the understanding of the physical processes underlying chemical lasers, as excursions outside the traditional operational parameter space become increasingly necessary.

## Problem and Methodology.

The objective of this work is to generate a greater physical understanding of the physical processes underlying COILs through use of the models employed in simulation of these devices. This objective is achieved through 3-D, time accurate numerical simulation of the COIL flowfield using the Navier-Stokes equations coupled to species continuity equations. Previous work by Madden and Miller[7] presented computational data for COIL simulation indicating that the flowfield should be marked by substantial flow unsteadiness, as documented in the experiments of Fric and Roshko[8] for incompressible, air-air jet-in-crossflows at Reynolds numbers similar to those found in COILs. Building on the earlier results, this work further elucidates the flow unsteadiness, the underlying physics, and the manifested effects in COIL performance.

The flow unsteadiness associated with the jet-in-crossflow interaction of the secondary He/I$_2$ injectors with the primary O$_2$($^1\Delta$) carrying flow leads to the generation of vortices that are transported downstream into the supersonic region where the laser cavity is located. These vortices through their rotation have associated velocity components that are parallel to optical axis, or the direction in which laser light passes back and forth during lasing. The motion of the bulk flow in the direction of the optical axis leads to Doppler broadening of the atomic iodine (I) $^2P_{1/2} \rightarrow ^2P_{3/2}$ transition lineshape. This effect is important in two ways: the first is the decrease in the line center gain of the $^2P_{1/2} \rightarrow ^2P_{3/2}$ transition and the second is in the breadth of the lineshape. The first effect is important relative to the performance of the laser, but the second effect is most important relative to the application of spectroscopic lineshape based diagnostics to the laser flowfield, as the I $^2P_{1/2} \rightarrow ^2P_{3/2}$ transition lineshape is frequently used to determine the gas temperature. Understanding the influence of the vortices upon the breadth of the I $^2P_{1/2} \rightarrow ^2P_{3/2}$ transition lineshape is thus important to understanding the accuracy of the temperature diagnostic in COIL experiments.

Relative to modeling of the gas flow through COIL devices, these flows can best be described as the translation of particles of different chemical composition with collisional interactions occurring between the particles and between the particles and the photons within the radiation field. Mathematically, this flow of particles is treated as a continuum and is approximated by Navier-Stokes continuity equations for mass, momentum, and energy. In integral form, these equations are given by:

$$\frac{\partial}{\partial t} \iiint\limits_{vol} \langle Q \rangle \, dvol + \oiint\limits_{A} (\vec{F} - \vec{F}_v) \cdot \hat{n} dA = \iiint\limits_{vol} \langle S \rangle \, dvol \qquad [1]$$

and the hyper vector of the conserved variables $\langle Q \rangle$ is:

$$\langle Q \rangle = \begin{vmatrix} \rho_1 \\ \vdots \\ \rho_N \\ \rho\vec{V} \\ \rho e_0 \end{vmatrix} = \begin{vmatrix} \rho_1 \\ \vdots \\ \rho_N \\ \rho u \\ \rho v \\ \rho w \\ \rho e_0 \end{vmatrix} \qquad [2]$$

The inviscid flux tensor, $\vec{F}$, the viscous flux tensor, $\vec{F}_v$, and the hyper vector $\langle S \rangle$ of sources for the production and loss of the reacting species are:

$$\vec{F} = \vec{V}\langle Q\rangle + \begin{vmatrix} 0 \\ \vdots \\ 0 \\ \overline{\overline{I}} \\ \vec{V} \end{vmatrix} P = \begin{vmatrix} \rho_1 \vec{V} \\ \vdots \\ \rho_N \vec{V} \\ \rho\vec{V}\times\vec{V} + P\overline{\overline{I}} \\ \rho\vec{V}h_0 \end{vmatrix}$$
[3]

$$\vec{F}_v = \begin{vmatrix} \rho_1 \vec{v}_1 \\ \vdots \\ \rho_N \vec{v}_N \\ \overline{\overline{\tau}} \\ \overline{\overline{\tau}}\cdot\vec{V} + \vec{\nabla}\cdot\vec{q} \end{vmatrix}$$
[4]

$$\langle S\rangle = \begin{vmatrix} \dot{\rho}_1 \\ \vdots \\ \dot{\rho}_N \\ 0 \\ 0 \end{vmatrix}$$
[5]

The production rates due to chemical reaction of the species $\rho_i$ are determined for each species continuity equation source by:

$$\dot{\rho}_{chem,i} = m_i \sum_{j=1}^{M} v''_{ij} - v'_{ij} \left[ k_{f,j}\prod_{k=1}^{N}\left(\frac{\rho_k}{m_k}\right)^{v'_{k,j}} - k_{b,j}\prod_{k=1}^{N}\left(\frac{\rho_k}{m_k}\right)^{v''_{k,j}} \right]$$
[6]

where the forward production rates of each reaction are determined from the Arrhenius rate law and the backward rates determined from the equilibrium and forward rates:

$$k_{f,j} = a_{f,j}T^{b_{f,j}}e^{\frac{e_{a_{f,j}}}{T}}$$
[7]

$$K_{eq,j} = \frac{k_{f,j}}{k_{b,j}}$$
[8]

$$K_{eq,j} = \left(\frac{P}{RT}\right)^{v''_{ij}-v'_{ij}} \exp\left(-\sum_{i=1}^{N}\frac{v''_{ij}-v'_{ij}}{R_i T}g_{0,i}\right)$$
[9]

Accurate description of molecular diffusion of chemically reacting species is important in the low pressure flowfields of chemical lasers. The Ramshaw-Dukowicz[9] approximation for multi-component diffusive transport is used as opposed to higher order approximations due to the minimal loss in accuracy and lower computational cost with respect to the higher order methods. These equations, including both concentration and pressure gradient contributions are given by:

$$\rho_i \vec{v}_i = -nm_i D_{im}\left[\frac{\partial \chi_i}{\partial \vec{r}} + \chi_i - f_i \frac{\partial \ln P}{\partial \vec{r}}\right]$$
$$+ f_i n\sum_{j=1}^{N} m_j D_{jm}\left[\frac{\partial \chi}{\partial \vec{r}} + \chi_j - f_j \frac{\partial \ln P}{\partial \vec{r}}\right]$$
[10]

Finally, the key laser quantity of gain is determined from the flowfield solution using the equations:

$$\alpha \, v_0 = \frac{7}{12}\left(\frac{A\lambda_0{}^2}{8\pi}\right)\phi \, v_0 \left(N_{I(^2P_{1/2})} - \frac{1}{2}N_{I(^2P_{3/2})}\right) \qquad [11]$$

$$\phi \, \omega \, v = \left[\left(\frac{a^2\,4\ln 2}{\pi^3}\right)^{1/2}\frac{1}{\Delta v_D}\right]\int_{-\infty}^{+\infty}\frac{e^{-y^2}}{\omega - y\,^2 + a^2}dy \qquad [12]$$

$$\omega = \frac{2\left(v - v_0\left(1+\dfrac{W}{c}\right)\right)}{\Delta v_D}\sqrt{\ln 2} \qquad [13]$$

$$a = \frac{\Delta v_L}{\Delta v_D}\sqrt{\ln 2} \qquad [14]$$

$$y = \frac{2v_z v_0}{c\Delta v_D}\sqrt{\ln 2} \qquad [15]$$

$$\Delta v_D = \frac{2}{\lambda}\sqrt{\frac{2RT\ell n2}{m_I}} \qquad [16]$$

$$\Delta v_L = \frac{T_{ref}}{T}P\sum_{i=1}^{N}\alpha_i\chi_i \qquad [17]$$

The computational fluid dynamics (CFD) code GASP from AeroSoft, Inc. is employed to solve equations [1]-[10] for the simulations performed here. GASP employs domain decomposition for distribution of the computation amongst multiple processors on parallel architectures, with inner-iteration methods used to maintain fully implicit, time accurate integration of the solutions.

The GASP COIL model utilizes 10 to 13 species mass conservation equations for the chemically reacting components of the COIL flow, depending upon the COIL model used, in addition to the base conservation equations for momentum and energy. An effective binary diffusion model is used to describe concentration and pressure contributions to mass diffusion, an important process in the low density COIL flowfield. 10 species, 22 reaction and 13 species, 52 reactions finite-rate chemistry mechanisms[10] are used to model the gas phase chemical kinetic processes that generate the population inversion in atomic iodine necessary for laser oscillation in COIL.

The computational grid used for the COIL simulations consists of 29 blocks and 8.1 million grid cells. The computational domain which this grid discretizes represents the smallest geometrically similar element within the COIL experiment flowfield hardware, denoted a 'unit-domain.' The unit-domain consists of a supersonic (M~2.2) converging-diverging nozzle section with one large and two small injector orifices that issue reactants into the primary flow through this nozzle. It was previously shown[11] that this particular configuration of the 'unit-domain' as opposed to one half as wide splitting the large injector orifice is necessary to properly capture unsteady fluctuations in the lateral or Z direction relative to Figure 1. Fig. 1 illustrates the unit-domain computational grid within the context of a surface rendering of the experiment's mixing nozzle. The orifices inject a sonic mixture of He and $I_2$ into a subsonic primary flow composed of He, $O_2(^1\Delta)$, $O_2(^3\Sigma)$, $H_2O$, and $Cl_2$ inducing the complex 3-D flow structure as the jet issuing from the orifice interacts with the crossflow. It is the combination of the interfacial area created by the complex 3-D flow structure and molecular diffusion that mixes the two flows. Boundary conditions accomplish the unit-domain approximation through the enforcement of planar symmetry at the nozzle centerline in the vertical direction and the side boundaries in the lateral direction treated as periodic surfaces with the outflow from one surface issuing into its' opposite and vice-versa. No-slip constant temperature boundary conditions are used at the wetted surfaces of the nozzle and orifices, with the temperature fixed at 400 K at the orifice region walls and 300 K at the nozzle walls. The nozzle and injector subsonic inflow boundary conditions fix the total pressure, total temperature, and the species fractions at constant values, while the derivative of the static pressure is set to 0. The nozzle outflow boundary condition sets the second derivative of the dependent variables to 0 as is appropriate for supersonic flows.

Two COIL chemistry models are tested on this grid to determine the effect of varying fidelity within the chemical reaction mechanism upon the laser gain prediction. The models tested include a 10 species, 22 reaction COIL chemistry

mechanism and a more detailed 13 species, 52 reaction COIL mechanism that is a superset of the smaller mechanism. References providing additional details beyond the scope of this paper may be found in Madden et al.[12,13]

### Results.

We begin by reviewing and updating previous results from unsteady simulation of COIL. A 3-D GASP model for the COIL flowfield was executed in time accurate mode utilizing 1st order accurate time integration and 3rd order spatial accuracy with a physical time step of $1.0 \times 10^{-9}$ sec in the 10 species, 22 reaction COIL chemistry mechanism simulation and $4.0 \times 10^{-9}$ sec in the 13 species, 52 reaction chemistry mechanism simulation. These time steps are somewhat lower than the time step of $1.0 \times 10^{-8}$ sec previously reported in these investigations, and were experimentally determined by reducing the time step until stable execution was obtained. The computation was advanced to a physical time of 0.00014 sec, corresponding to 143,800 time steps in the 10 species, 22 reaction simulation and 0.00064 sec, corresponding to 159,500 time steps in the 13 species, 52 reaction simulation. The physical times of 0.00014 sec and greater provide sufficient temporal advancement of the computations to address the characteristics of the predicted flow unsteadiness.

The time accurate execution of the GASP COIL model generated a prediction of flow unsteadiness that did not decay over the time intervals that the computations were advanced. The unsteadiness was found to extend from the jet/primary interaction region at the point of the He/$I_2$ transverse injection and continue downstream undiminished. Fig. 2 illustrates the resulting impact of the flow unsteadiness upon the structure of the flow within the He/$I_2$ jet. Here an isosurface of 0.085 constant total iodine ($I_2+I_2^*+I+I^*$) mass fraction is plotted within 3-D space. The surface demonstrates the presence of complex, periodic structures associated with the unsteady vortex generation, and indicates that there is a strong interaction between the fluid from the large and small orifices. The break-up of the jets occurs as the fluid from the small orifices begins to interact with that from the large, illustrated by the change in the surface structure from smooth with periodic fluctuations to the more complex structure associated with the break-up. Since molecular diffusion and chemical reactions are strongly correlated with spatial gradients of reactant concentration, the presence of these unsteady flow structures is expected to have considerable impact upon the predicted generation and variation of I and I$^*$, the end products of the chemistry mechanisms. The gain given by equation [11] is directly proportional to the number densities of I and I$^*$, the end products of the chemistry mechanism, thus the correlation between gain and the flow structure as shown in Fig. 3 illustrates this point.

The underlying sources of the flow unsteadiness are the 'wake vortices' in the flow behind the He/$I_2$ jets. These vortices have their origin in the primary flow boundary layer fluid that wraps around the orifice flow and project down from the wall with rotation, subsequently interacting with the jet fluid. Fig. 4 illustrates this with plots of streamlines originating in the boundary layer fluid upstream of the jet shown in conjunction with vortex cores. The cores were extracted using the vortex core identification functions of Sujudi and Haimes[14] implemented in the Tecplot visualization software from Amtec Engineering. The red vortex core traces can be found at the center of the swirls in the streamlines, identifying the presence of vortices. Two wake vortices are seen projecting downward from the wall immediately behind the large orifice, and a third projects downward from the wall in the center of the domain between the large and small injector orifices. Similarly, additional vortices are seen projecting downward from the wall behind the small injector orifices. Temporal variation of the flow fluctuations and Fourier analysis of these fluctuations for the two simulations is shown in Figs. 5-8. Fourier analysis of the fluctuations from the 10 species, 22 reaction simulation yielded frequencies of 56, 94, 131, and 150 kHz. The 13 species, 52 reaction simulation yielded frequencies of 12.1, 24.9, 42.3, 60.4, 96.6, 133.9, 151, and 292 kHz. The peak fluctuation amplitudes for the lateral velocities are 175 m/sec in both simulations. The presence of the unsteady fluctuations within the jet structure is consistent with the experimental literature on jet-in-crossflow interactions. In particular, the capture of the wake vortices as well as their location is entirely consistent with the experimental investigations, exemplified in the work of Frik and Rhosko.[8]

The objective of this investigation is to capture these fluctuations and quantify the impact upon the predicted Voigt lineshape of the I $^2P_{1/2} \rightarrow ^2P_{3/2}$ transition. The vortices associated with the jet unsteadiness will rotate in a manner such that the axis of rotation is orthogonal to the optical (Z) axis. Fig. 9 shows vertical and lateral plane cuts through the domain of the 13 species, 52 reaction COIL simulation, providing an illustration of some of these vortices. The scale of the vortices is such that large fractions of the gas will contribute to Doppler broadening of the lineshape transition. The optical (Z) axis or lateral velocity component $W$ influences the Voigt function for the transition lineshape $\phi$ through the dependence found in equations [12] and [13]. The magnitude of this impact is illustrated in Figs. 10 and 11. Fig. 10 shows the percentage change in the lineshape function $\phi$ at line center due to the influence of the velocity $W$ relative to the value of $\phi$ at line center without the velocity influence; representative thermodynamic conditions and species fractions within the exit plane of the simulations were used for this example. The exit plane of these simulations is physically located just upstream of the laser cavity, so performance impacts shown here are directly relevant to cavity

conditions. At velocity magnitudes of ±100 m/s the decrease in the line center value is 35% and at ±200 m/s the decrease is 80%, corresponding directly to a decrease in the line center gain. Fig. 11 shows the lineshape function $\phi$ variation with different values of the velocity $W$ between -200 and 200 m/s, again for thermodynamic conditions within the exit plane of the simulations. The shift in the lineshape position from left to right represents the change from -200 to 200 m/s. It is evident that a cumulative lineshape composed of all these various lineshapes would be a wider or broadened lineshape, depending upon the weighting given to each of the individual lineshapes. Figs. 12 and 13 illustrate the spatial variation of the $W$ velocity and fractional decrease in the gain within the exit plane at a single point in time from the 10 species, 22 reaction simulation. The correlation between the spatial variation of the $W$ velocity and the fractional gain decrease is clearly illustrated within these figures as local increases in the $W$ velocity magnitude lead to local deceases in the line center gain.

The end question to be answered here is 'what effect does the unsteady flow structure have upon the predicted lineshape?' This question is answered by accumulating a dataset containing the spatial and temporal variation of the quantities necessary to calculate the gain. This dataset is first spatially averaged in the Z axis direction and then temporally averaged, consistent with the behavior of a tunable diode small signal gain probe or lasing action over a period of time. Mathematically, this is expressed as:

$$\alpha_{ave}\left(\nu,y\right) = \frac{1}{t_{tot}z_{tot}}\iint \alpha\left(\nu,y,z,t\right)dzdt \qquad [18]$$

where $t_{tot}$ is the total time interval of the integration, $z_{tot}$ is the total distance of integration in the Z axis direction, and $\alpha(\nu,y,z,t)$ is determined using equations [11] - [16]. For the simulations performed here, the exit plane as shown in Fig. 13 was exported every 1.0e-07 sec of physical time, and the Z integration was performed along lines of constant Y. Figs. 14 and 15 show composite gain lineshapes versus normalized frequency in this plane for the 10 species, 13 reaction and 13 species, 52 reaction COIL simulations; the frequency axis is normalized to let the line center of the I $^2P_{1/2} \rightarrow {}^2P_{3/2}$ transition at $1.31527\mu m$ to be set to zero. Here $t_{tot}$ is $1.4\cdot10^{-04}$ sec for the 10 species, 22 reaction simulation and $6.4\cdot10^{-04}$ sec for the 13 species, 52 reaction simulation, and $z_{tot}$ is the full dimension in the z direction. The impact of the velocity component $W$ is upon lineshape is shown in these plots. The lineshape including the influence of the gas velocity is broadened somewhat and the line center gain is lower than the line shape without it, indicating lower amplification for the regions of the flowfield where the broadening effects of the velocity field are significant.

The measured transition lineshapes, as mentioned earlier, provide a tool for determining the concentration of species in the COIL flowfield, particularly that of the I atoms relevant to the purposes of this discussion. However, additional information can be extracted through the fitting of equations [11] - [16] to the measured lineshape. In COIL experiments this methodology is commonly utilized to determine the gas temperature, in conjunction with the assumption of no rotation of the bulk gas flow. This issue is not related to the work of Nikolaev et al[6] who used the asymmetric shift of the lineshape to one side or another of the line center as a means to determine the streamwise flow velocity. As shown in Figs. 14 and 15, the effect of the eddies within the flow over large periods of time relative to the characteristic timescales of fluctuation is to broaden the lineshape symmetrically in a manner that could be misinterpreted to be due to the random translational motion of the atoms as measured in temperature. The question that can be answered here is 'what is the error incurred in neglecting the influence of eddy rotation upon the lineshape when extracting temperatures from measured lineshapes?'

This question is answered here by fitting equation [11] to the spatially, temporally averaged lineshapes plotted in Figs. 14 and 15 using the assumption of all Doppler broadening to be due to random, thermal motion. This analysis allows the lineshapes to be treated as synthetic representations of experimentally measured lineshapes, with the absence and the presence of the bulk gas velocity influence in the lineshapes providing an independent parameter for quantifying the effect of bulk gas velocity in terms of temperature. To fit equation [11] to the spatially, temporally averaged lineshapes reduced from the unsteady simulations, the MINPACK[15] implementation of the Levenberg-Marquardt[16,17] nonlinear fit algorithm is used[18] to determine the best fit of [11] to the data as a function of a given set of fit parameters. Observing the form of functional form of equation [11], it is seen that it consists of a shape function $\phi(\nu)$ given by the Voigt function in equation [12], and an amplitude given by:

$$\frac{7}{12}\left(\frac{A\lambda_0^2}{8\pi}\right)\left(N_{I(^2P_{1/2})} - \frac{1}{2}N_{I(^2P_{3/2})}\right) \qquad [19]$$

Given that the Voigt represents the probability versus frequency, the infinite integral is 1.

$$\int_{-\infty}^{+\infty} \varphi(\nu)d\nu = 1 \tag{20}$$

Integrating [11] allows for determination of [19] and separation of the Voigt from the lineshape:

$$\int_{-\infty}^{+\infty} \alpha\left(\nu\right) d\nu = \int_{-\infty}^{+\infty} \frac{7}{12}\left(\frac{A\lambda_0{}^2}{8\pi}\right)\phi\left(\nu\right)\left(N_{I(^2P_{1/2})} - \frac{1}{2}N_{I(^2P_{3/2})}\right)d\nu$$

$$= \frac{7}{12}\left(\frac{A\lambda_0{}^2}{8\pi}\right)\left(N_{I(^2P_{1/2})} - \frac{1}{2}N_{I(^2P_{3/2})}\right) \tag{21}$$

and

$$\alpha\left(\nu\right) = \varphi(\nu)\int_{-\infty}^{+\infty} \alpha\left(\nu\right) d\nu \tag{22}$$

Thus the individual values of the gain $\alpha(\nu)$ at each $\nu$ can be normalized by the infinite integral over the lineshape, recovering the probability aspect of the Voigt. However, in practice it was found that this method for fitting the lineshape introduced error because the integral bounds are limited to the frequency domain of the lineshapes, which are $\pm 1.75$ GHz about the line center and not infinite as required by [20]. This introduces an error in the fit such that evaluation of equation [23] via [24] is 0.99, not 1.0. This error translated into a 5 K error in the temperature determination, and was subsequently determined to be avoidable if [25] were treated as a separate fitting parameter. In practical terms, the fitting function becomes:

$$\alpha\left(\nu,\Delta\nu_D,\Delta\nu_L\right) = \beta\varphi(\nu,\Delta\nu_D,\Delta\nu_L) \tag{26}$$

where $\beta$, $\Delta\nu_D$, and $\Delta\nu_L$ are the fitting parameters used in the nonlinear fit. With the values for the Doppler and Lorentzian widths $\Delta\nu_D$ and $\Delta\nu_L$ determined, separate values for the temperature can be found using equations [16] and [17] and an independent determination of the pressure and the mole fractions. Here, the simulation data were spatially and temporally averaged using the same procedure as for the gain expressed mathematically in equation [18] to determine average pressures and species mole fractions. When performing this analysis with experimentally measured lineshapes, wall pressures and mean mole fractions based upon the measured molar flow rates may be the only values available and may lead to errors in the extracted temperatures.

The degree of agreement between the Doppler and Lorentzian determined temperatures and the average thermodynamic temperature from the simulation provides a means to assess the lineshape fit and the interpretation of the fit. To perform this comparison, the thermodynamic temperatures were averaged from the simulation data using the same integration procedure as used for the gain in equation [18]. Figs. 16 - 19 show the temperatures from the lineshape fit determined values for the Doppler and Lorentzian widths and the averaged thermodynamic temperature from the simulations. Figs. 16 and 17 show the temperatures for the fits for the 10 species, 13 reaction and 13 species, 52 reaction simulation extracted lineshapes in which the bulk gas velocity was not included in the functional evaluation of equations [11] and [18]. The agreement between the Doppler, Lorentzian, and thermodynamic temperatures shown in Figs. 16 and 17 is very close, to within 1%, as should occur, providing a verification of the fitting procedure. When the temperatures are determined for the lineshapes in which the bulk velocity was directly included in the functional evaluation of equations [11] and [18], as shown in Figs. 18 and 19, the Doppler temperature diverges from the Lorentzian and thermodynamic temperatures in the flow regions closer to the nozzle centerline, with the maximum difference being 14 K. This trend is consistent with the observation that the unsteady eddies increase in size and strength toward the center of the nozzle as illustrated in Fig. 2. Thus the Doppler temperature is registering the clear influence of the bulk gas velocity, whereas the Lorentzian temperature remains consistent with the thermodynamic temperature. Given the results illustrated here, a suggested method of lineshape fitting in experimentally measured lineshapes where signal-to-noise can interfere with the nonlinear fitting would be to fix the Lorentzian width based upon an independent temperature measurement such as a rotational temperature, and then determine the Doppler width. Then the degree to which the Doppler temperature differs from the rotational or other temperature measurement would be an indicator of the magnitude of flow rotation. It should be noted that fitting procedures in which the Doppler and Lorentzian component temperatures are forced to be equal, as is commonly done, could very well be masking information regarding the degree of eddy strength and flow unsteadiness in the experiments. A suggested test would be to re-visit existing lineshape

temperature determinations for experiments in which flow unsteadiness and eddy generation could potentially be present, and perform the nonlinear fit without fixing either the Doppler and Lorentzian component. The difference in temperatures could then be correlated against fluid dynamic parameters relevant to eddy generation such as Reynolds number to determine the presence of trends.

The temperature determination from the averaged lineshapes illustrated the sensitivity of the temperature determination process to the magnitude of the flow velocity components. Observing the decrease in grid density within the nozzle expansion in Fig. 1 and the dissipation of the vortices within Fig. 9, it is reasonable to question whether the increase in grid cell size with streamwise distance in the expansion is filtering the smaller eddies as well as decreasing the strength of the eddies through numerical dissipation. Fig. 20 illustrates this point through the plotting of a constant vorticity isosurface with a value of $2.0 \cdot 10^5$ s$^{-1}$. The figure shows that this particular vorticity magnitude, while persistent within the freestream before the nozzle throat, disappears rapidly as the flow passes through the throat. This decrease is consistent not just with the decrease in grid density but also with the physical effect of the flow expansion and the commensurate stretching of the vortices. To separate the effect of flow dilation upon vorticity from that of grid dissipation, it is necessary to decrease grid dissipation by increasing the grid resolution.

The effect of grid dissipation upon the transport of vorticity in the nozzle expansion and the subsequent effect upon the lineshape is examined by quadrupling the number of grid cells in the streamwise direction within the nozzle expansion while keeping the number of cells in the transverse directions constant. This increases the number of cells in the streamwise direction from 128 to 512. This new grid is used to continue the 13 species, 52 reaction mechanism simulation and accumulate sufficient temporal information regarding the influence of the unsteadiness upon the lineshape. The simulation was advanced for an additional 91,000 time steps with a step size of $2.0 \cdot 10^{-9}$ s, limited by solution stability. Data necessary for the lineshape analysis were collected within the same plane transverse to the flow as was previously used.

The first point of examination of the effect of increased grid resolution is the vorticity. The isosurface of constant total vorticity at a value of $2.0 \cdot 10^5$ s$^{-1}$ previously plotted in Fig. 20 for the original grid is now generated for the new grid and plotted in Fig. 21. The first and most obvious feature distinguishing the two plots is that the vorticity loss within the downstream end of the nozzle expansion found in the simulation using the original grid does not appear in the simulation using the higher cell density grid, confirming that the grid is impacting the transport of the flow fluctuations in this region. While vorticity is a measure of flow rotation and is associated with the velocity components in the lateral direction that influence the lineshape, it is also correlated with mixing and the grid resolution effect shown here would be expected to extend beyond the broadening to the general prediction of the COIL flowfield.

The lateral $W$ velocity component that contributes to the lineshape broadening is examined within the planar cut of the nozzle shown previously from the standpoint of the maximum and minimum values predicted during the period of the simulation and from the perspective of the RMS variations relative to the average over this same period. The minimum and maximum values of the $W$ velocity component predicted within this plane for each $Y, Z$ position within the physical time of the simulation for both the original and new grid are shown in Figs. 22-25. In these plots, the absolute value of the minimum and maximum $W$ velocity is seen to be considerably higher over a greater area of the flow in the results from the simulation using the higher density grid as opposed to those from the simulation using the original grid. In other words, the predicted peak magnitude of the lateral fluctuations in the nozzle expansion as expressed in terms of the $W$ velocity is higher in high density grid simulation than in the original grid simulation. An RMS examination of the $W$ velocity variation relative to the average over the period of the simulations provides a means to measure the pervasiveness of the $W$ velocity fluctuations over time. Observing the values within Figs. 26 and 27, it is seen that the values are relatively low, less than 1 m/s for both simulations. This occurs because the differences from the average are weighted with respect to time and with the fluctuations being transitory the RMS difference values are substantially less than the peak values. Comparing the RMS difference for the $W$ velocity component within the plane, it is seen that the peak values from the high density grid simulation are almost a factor of 2 greater than the simulation from the original grid. Additionally, the area covered by these peak values is much greater for the new simulation, implying that the effect upon the lineshape should be greater and more persistent across the nozzle than in the original grid simulation.

An examination of the Doppler and Lorentzian temperature components based upon fitting of the lineshapes for the original and higher resolution grid simulations provides the final point of comparison. Fig. 28 shows the Doppler, Lorentzian, and thermodynamic temperatures for the new grid simulation compared with the Doppler temperature from the original grid simulation. Comparing the Doppler temperatures, the values from the higher density grid simulation are somewhat higher over a greater section of the nozzle than the original grid, consistent with the analysis performed above. Additionally, the maximum difference between the Doppler and Lorentzian temperatures for the new grid simulation is 24 K, an increase from 14 K for the original simulation. This confirms the hypothesis that the grid

resolution impacts the lineshape analysis and strengthens the argument that flow unsteadiness is a factor in temperature extraction for lineshapes in these flows.

An auxiliary issue that is addressed by this investigation is the predictive differences between the 10 species, 22 reaction COIL chemistry mechanism and the more detailed 13 species, 52 reaction COIL chemistry mechanism within the context of the unsteady 3-D simulation. Figs. 29 and 30 show the spatially and temporally averaged thermodynamic temperature and line center gains within the exit plane of the simulation, just upstream of the laser cavity. The temperature values are close, with the simulation using the 13 species, 52 reaction mechanism giving slightly higher values than that using the 10 species, 22 reaction mechanism, consistent with the presence of additional quenching reactions in the more detailed mechanism. The values for the line center gain are somewhat different, however. While similar in profile and value for the upper half of the nozzle above 0.004 m, the profile and values are somewhat different in the lower half where the eddies are most dominant. This indicates that the increased mixing associated with the greater interfacial area across the eddies is coupling to the additional reaction pathways found in the more detailed 13 species, 52 reaction mechanism, leading to differences in the predicted gain.

### Summary and Conclusions.

In conclusion, the results provided here predict that the bulk gas flow velocity components associated with vortex rotation will broaden the lineshape for quantum transitions of species within the gas flow. The studies performed here show that if the bulk gas velocity influence is ignored when fitting the lineshape and the velocities are present, the effect will be a divergence between the reduced Doppler and Lorentzian values of the temperature. The results found here indicate that this difference may be as high as 24 K. Based upon the observed decrease in vorticity within the nozzle expansion in conjunction with decreased grid density, an additional simulation was performed that increased the grid in the streamwise direction in this region by a factor of 4. Comparing the results from the simulations from different grids, the higher density grid dramatically decreased dissipation of vorticity, captured higher magnitude velocity amplitudes, and showed a 10 K increase between the Doppler and Lorentzian temperatures over the original grid simulation. Based upon the observed trends in temperature prediction, it is suggested that the difference between the temperatures extracted from the fit values for the Doppler and Lorentzian widths could be correlated against changes in fluid dynamic parameters such as Reynolds number to determine trends.

A comparison of line center gain predictions from the simulations shows differences between the predictions of the 10 species, 22 reaction COIL chemistry mechanism and the more detailed 13 species, 52 reaction mechanism. It was observed that the differences were most pronounced in regions where the eddy strength was greatest, correlating with the enhanced mixing in this region.

### References.

[1] Struve, O. and Elvey, C. T., "The Intensities of Stellar Absorption Lines," *Astrophysical Journal*, **79**, pp. 409-440, 1934.

[2] Allen, MG., Carleton, K.L., Davis, S.J., Kessler, W. J., and McManus, K. R., "Diode laser-based measurements of water vapor and ground state oxygen in chemical oxygen iodine lasers," AIAA-1994-2433, *25th AIAA Plasmadynamics and Lasers Conference*, Colorado Springs, CO, 1994.

[3] Davis, S. J., Allen, M. G., Kessler, W. J., McManus, K. R., Miller, M. F., and Muihall, P. A., "Diode laser-based sensors for chemical oxygen iodine lasers," Paper 2702-18, *Proceedings of SPIE Conference on Gas and Chemical Lasers*, **2702**, pp. 195-201, San Jose, CA, 1996.

[4] Davis, S. J., Kessler, W. J., Bachmann, M., and Mulhall, P.A., "Collisional broadening coefficients for oxygen and water absorption lines used in COIL diagnostics," Paper 3268-80, *Proceedings of SPIE Conference on Gas and ChemicalLasers*, **3268**, pp. 218-226, San Jose, CA, 1998.

[5] Davis, S. J., Kessler, W. J., and Keating, P. B., "Progress in the development of sensors for COIL devices," *Proceedings of SPIE Conference on Gas, Chemical, and Electrical Lasers and Intense Beam Control and Applications*, **3931**, pp. 156-161, 2000.

[6] Nikolaev, V.D., Zagidullin, M. V., Svistun, M. I., Anderson, B. T., Tate, R. F., and Hager, G. D., "Results of Small-Signal Gain Measurements on a Supersonic Chemical Oxygen Iodine Laser with an Advanced Nozzle Bank." *IEEE Journal of Quantum Electronics*, **38**, no. 5, May 2002.

[7] Madden, T. J. and Miller, J. H., "Simulation of Flow Unsteadiness in Chemical Laser Flowfields," AIAA-2004-0805. *42nd AIAA Aerospace Sciences Meeting and Exhibit*, Reno, NV, 5-8 Jan, 2004.

[8] Fric, T. F., and Roshko, A., "Vortical structure in the wake of a transverse jet," *J. Fluid Mech*, **279,** pp. 1-47, 1994.

[9] Ramshaw, J. D. and Dukowicz, J. K., "APACHE: A Generalized Mesh Eulerian Computer Code for Multicomponent Chemically Reactive Fluid Flow," Los Alamos Report LA-7427, Jan. 1979.

[10] Perram, G. P, .*Int. J. Chem. Kinet*. **27**, 817-28 (1995).

[11] Madden, T. J. "An Analysis of Mechanisms Underlying Flow Unsteadiness in Chemical Oxygen-Iodine Laser Mixing Systems," AIAA-2005-5390, *36th AIAA Plasmadynamics and Lasers Conference*, Toronto, Ontario, Canada, June 6-9, 2005.

[12] Madden, T. J. and Solomon, W. C., AIAA 97-2387, *28th Plasmadyamics and Lasers Conference*, Atlanta, GA, June 23-25, 1997.

[13] Madden, T. J., *SPIE Proceedings of XIVth International Symposium On Gas Flow & Chemical Lasers and High Power Laser Conference*, Wrocław, Poland, 25-30 August, 2002.

[14] Sujudi, D. and Haimes, R., "Identification of Swirling Flow in 3-D Vector Fields," AIAA Paper 95-1715, *12th AIAA Computational Fluid Dynamics Conference and Open Forum*, San Diego CA, 19-22 June 1995.

[15] www.netlib.org/minpack.

[16] Levenberg, K. "A Method for the Solution of Certain Problems in Least Squares," *Quart. Appl. Math*. **2**, pp. 164-168, 1944.

[17] Marquardt, D. "An Algorithm for Least-Squares Estimation of Nonlinear Parameters" *SIAM J. Appl. Math*. **11**, pp. 431-441, 1963.

[18] Keating, P. B., private communication, Sept. 1998.
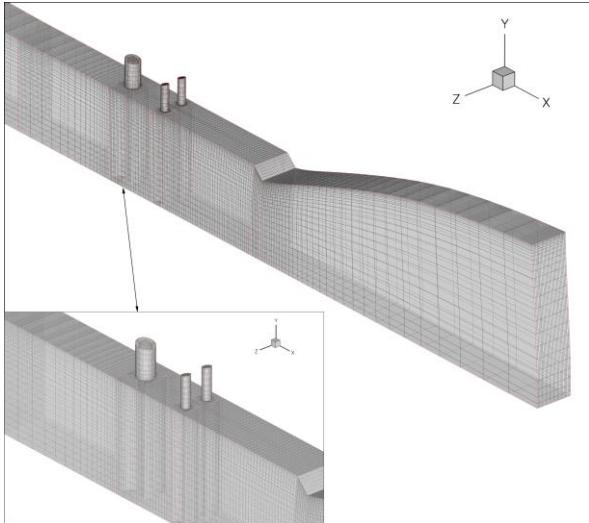
Figure 1. Computational grid used in the 3-D GASP simulations of COIL hardware, shown in relation to a rendering of the wetted surfaces in the COIL laser hardware. Note that the resolution show here is 1/64th that used in the execution of the simulation.
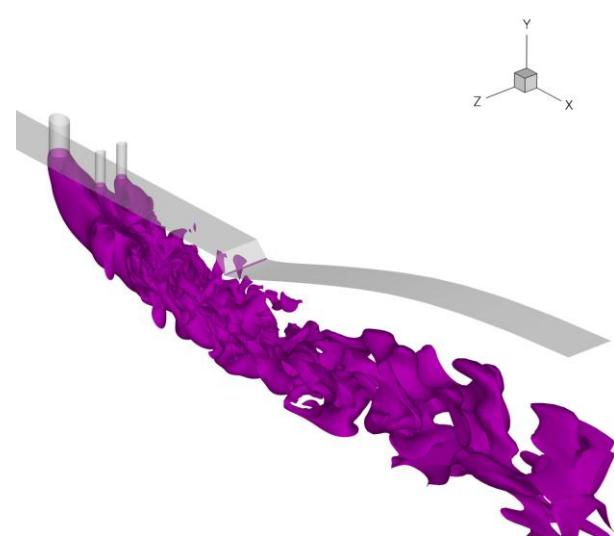


Figure 2. Fixed time snap shot of the unsteady fluid dynamic structures manifested in the He/$I_2$ jet from the 10 species, 22 reaction 3-D GASP COIL simulation. A surface of constant total iodine mass fraction, value = 0.085, acts as a scalar tracer for the jet structure.
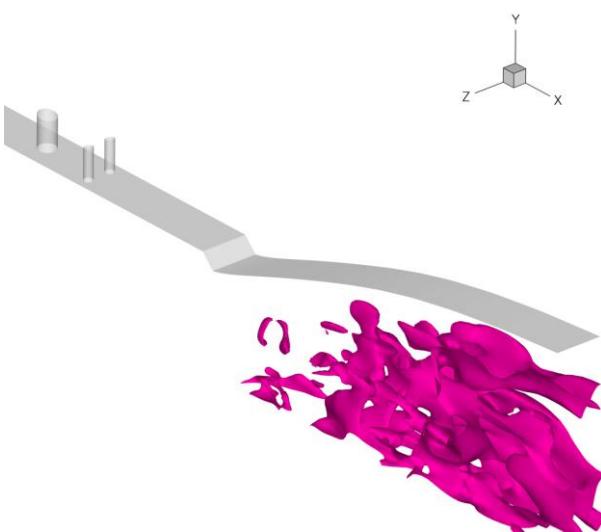


Figure 3. Fixed time snap shot of an isosurface of constant gain, value = 0.3 %/cm, from the 10 species, 22 reaction 3-D GASP COIL simulation illustrating the explicit dependence of laser gain on flow structure.
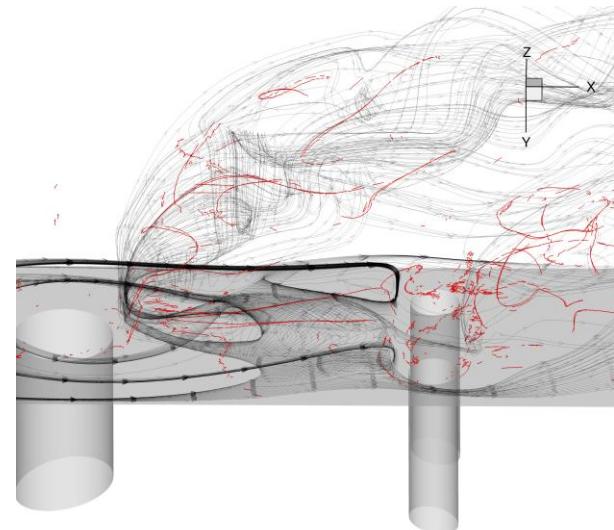


Figure 4. 3-D streamtraces (in black) initiated upstream of the large injector orifice 2% of the channel height from the wall in conjunction with vortex cores (in red) extracted from the 10 species, 22 reaction 3-D GASP COIL simulation.
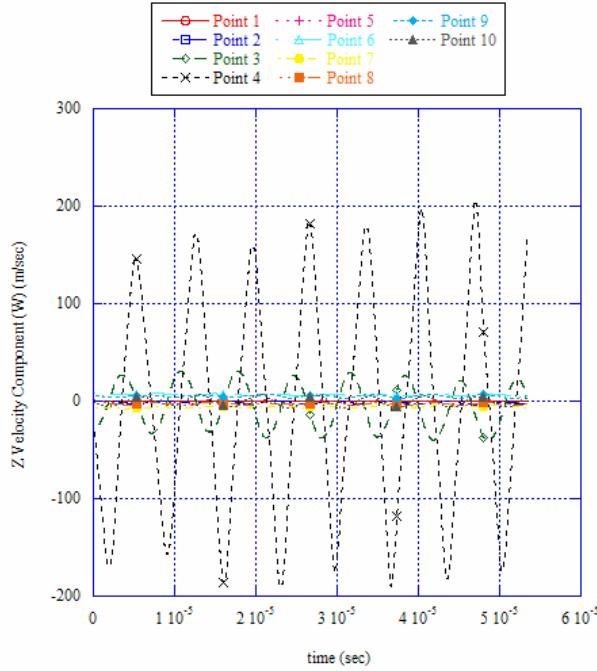
Figure 5. Time variance of the lateral velocity (Z) component at various monitoring points in the jet nearfield from the 8 million grid cell, 10 species, 22 reaction COIL hardware simulation.
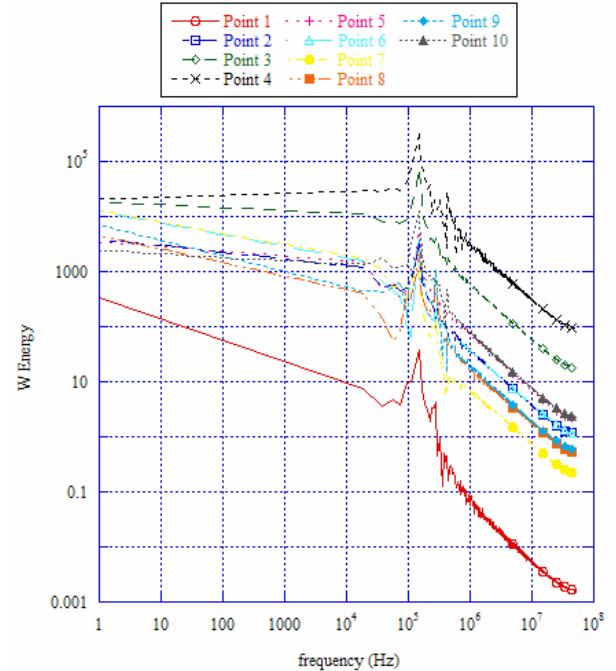


Figure 6. Fourier analysis of the lateral velocity (Z) component in Fig. 5.
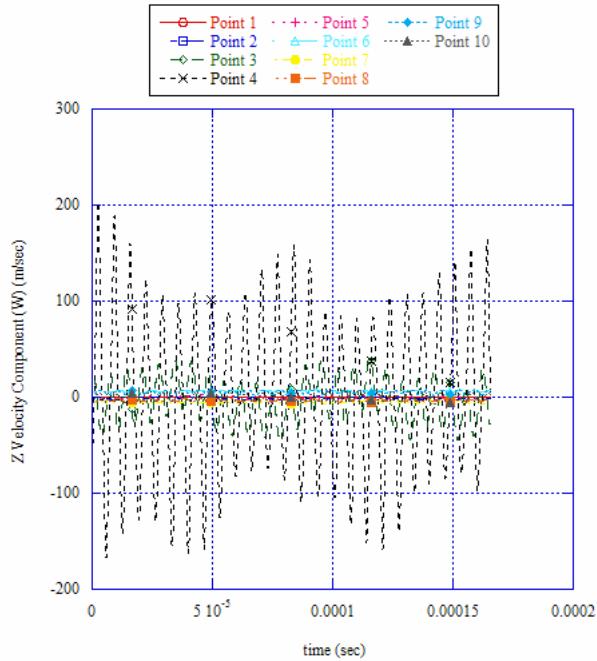


Figure 7. Time variance of the lateral velocity (Z) component at various monitoring points in the jet nearfield from the 8 million grid cell, 13 species, 52 reaction COIL hardware simulation.
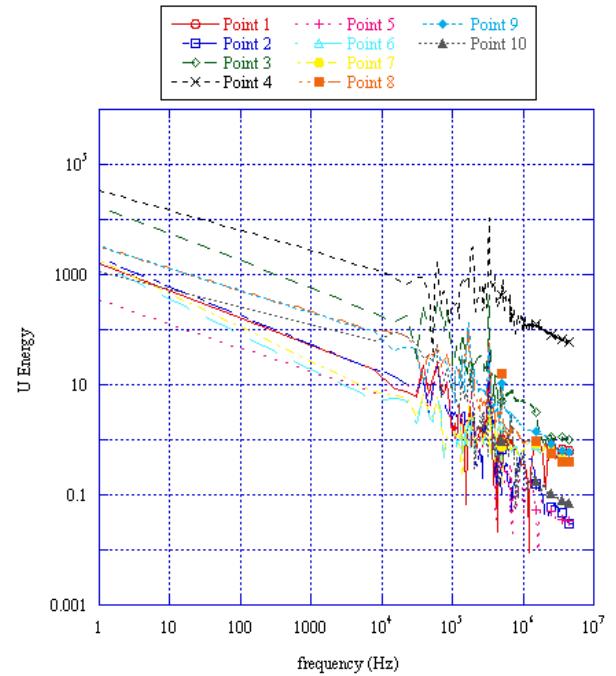


Figure 8. Fourier analysis of temporal variation of the streamwise or Z direction velocity (W) component in Fig. 7.

American Institute of Aeronautics and Astronautics
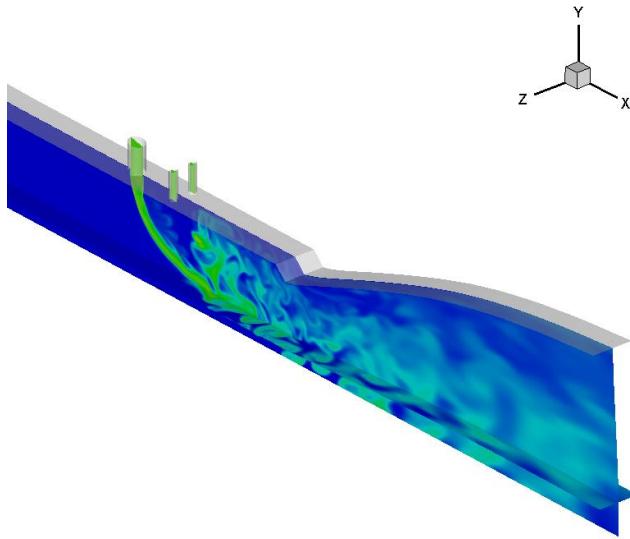
Figure 9. I$_2$ mole fraction distribution within 2-D. planes in the the 8 million grid cell, 13 species, 52 reaction COIL hardware simulation illustrating flow structure and fluctuation structure.
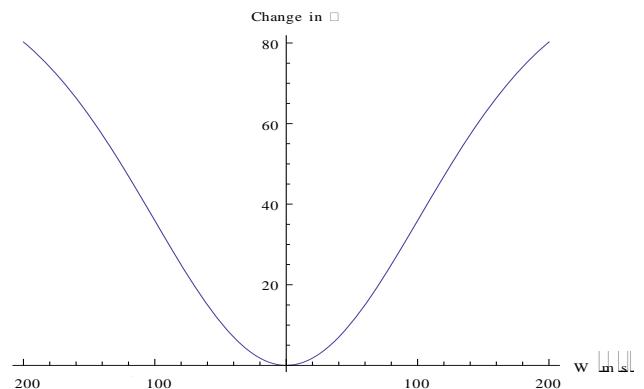


Figure 10. Percentage decrease in the lineshape function $\phi$ at line center due to the influence of the optical axis velocity component $W$ for thermodynamic conditions and species fractions within the exit plane of the simulations.
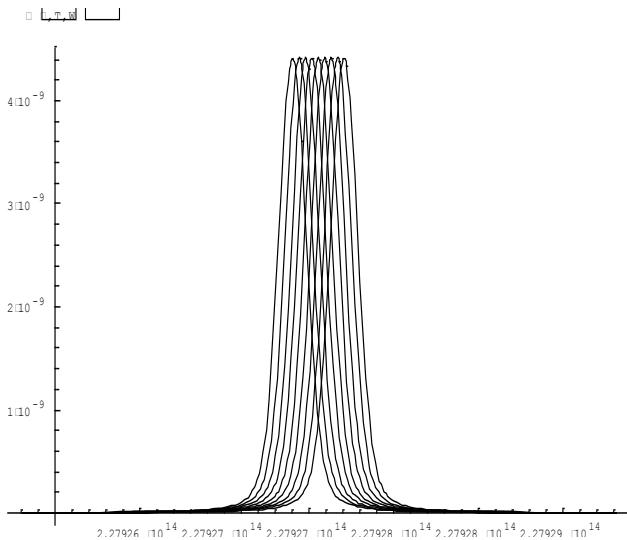


Figure 11. Lineshape distribution for $W$ velocity components from -200 to 200 m/sec, separated by increments of 50 m/sec. The shift from left to right corresponds with changing velocity from -200 to 200 m/sec.
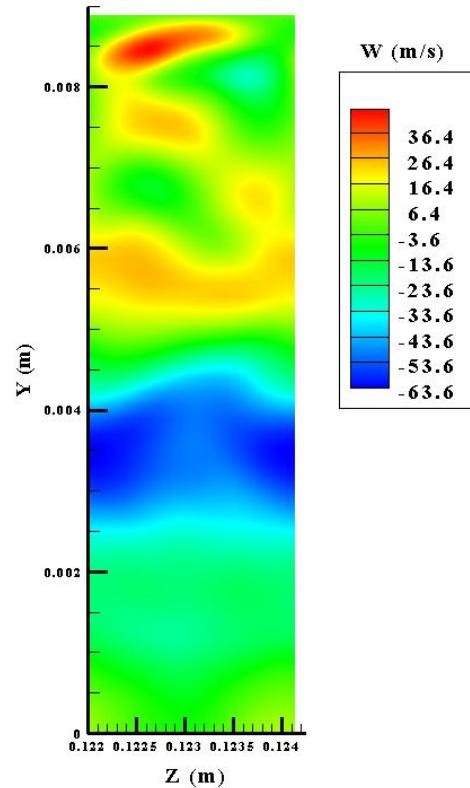


Figure 12. Time slice of $W$ velocity component within exit plane of the 13 species, 52 reaction simulation.

13
American Institute of Aeronautics and Astronautics
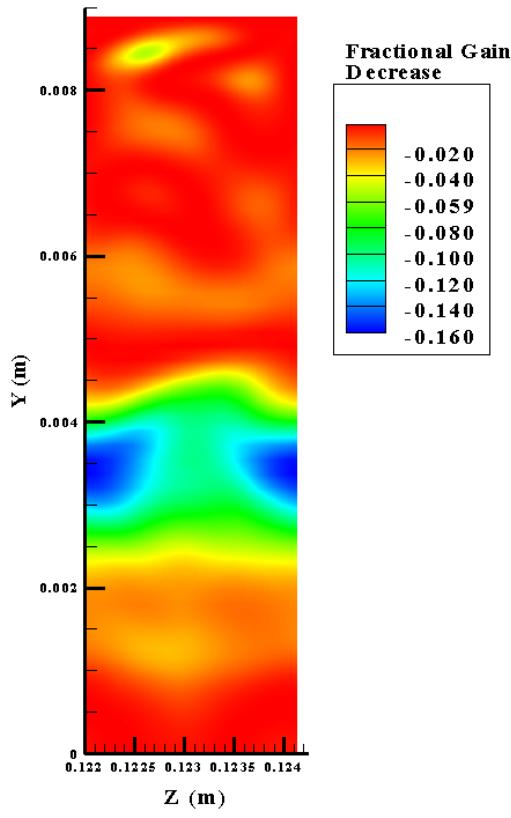
Figure 13. Fractional decrease in the gain calculation with the *W* velocity component relative to the gain calculation without within a time slice in the exit plane of the 13 species, 52 reaction simulation.



Figure 14. Time, space averaged gain lineshape from the 8 million grid cell, 10 species, 22 reaction COIL simulation.
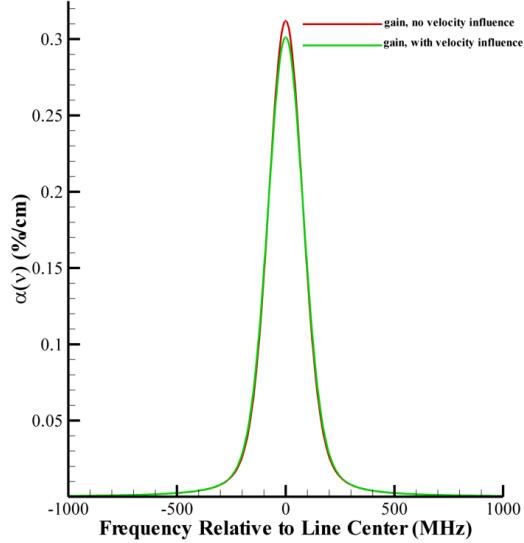


Figure 15. Time, space averaged gain lineshape from the 8 million grid cell, 13 species, 52 reaction COIL simulation.
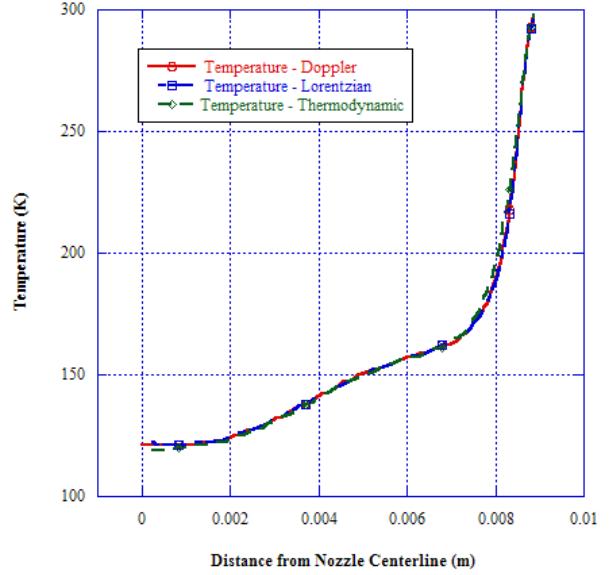


Figure 16. Comparison of temperature values from the 10 species, 22 reaction simulation; Doppler and Lorentzian values were determined based upon the lineshape in Fig. 14 without the velocity dependence and the thermodynamic values averaged from the simulation data. The horizontal axis is Y, the coordinate orthogonal to the flow direction and the nozzle wall

American Institute of Aeronautics and Astronautics
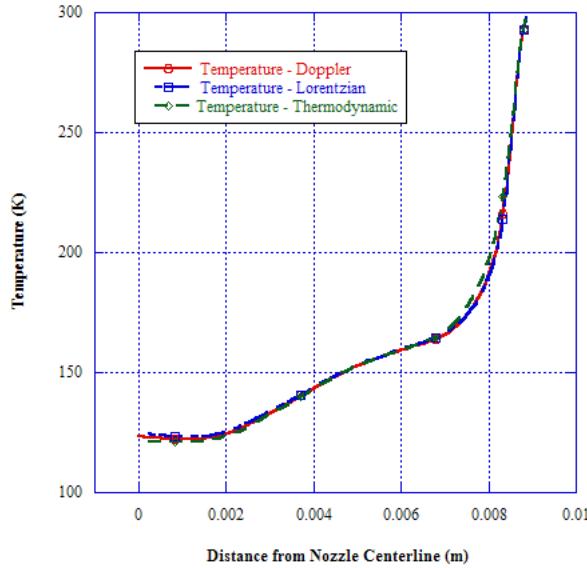
Figure 17. Comparison of temperature values from the 13 species, 52 reaction simulation; Doppler and Lorentzian values were determined based upon the lineshape in Fig. 15 without the velocity dependence and the thermodynamic values averaged from the simulation data.
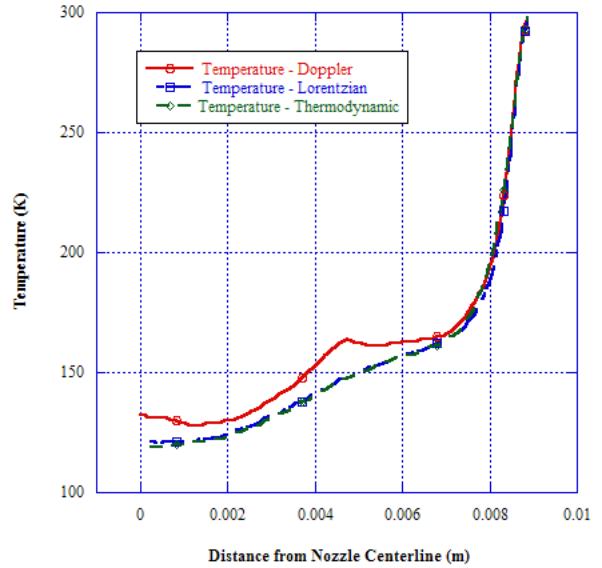


Figure 18. Comparison of temperature values from the 10 species, 22 reaction simulation; Doppler and Lorentzian values were determined based upon the lineshape in Fig. 14 with the velocity dependence and the thermodynamic values averaged from the simulation data.
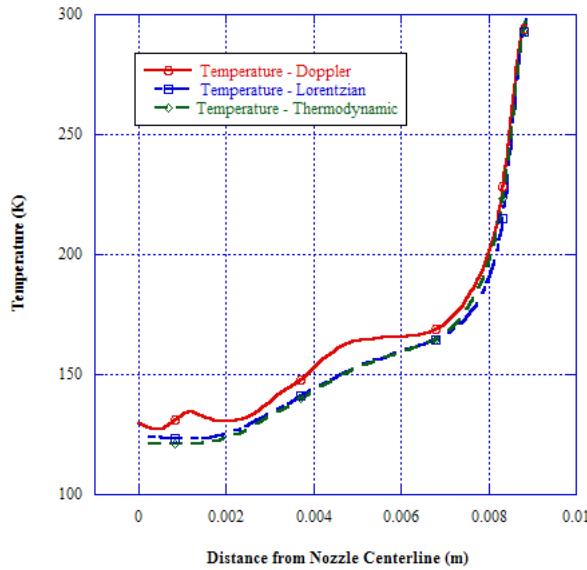


Figure 19. Comparison of temperature values from the 13 species, 52 reaction simulation; Doppler and Lorentzian values were determined based upon the lineshape in Fig. 15 with the velocity dependence and the thermodynamic values averaged from the simulation data.
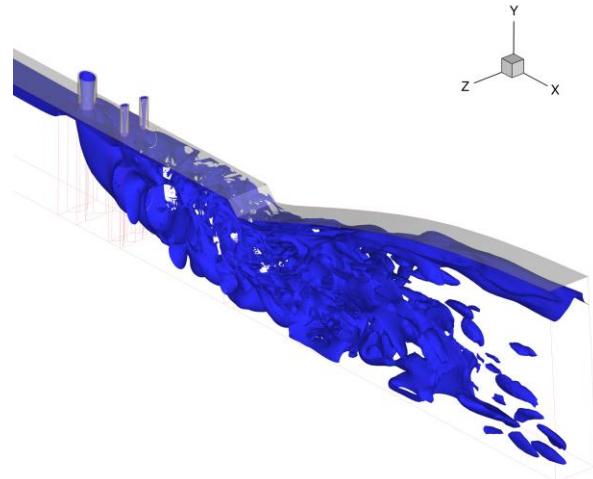


Figure 20. An isosurface of constant total vorticity with a value of $2.0 \cdot 10^5$ (1/s). This simulation used 128 points in the streamwise direction in the grid within the nozzle expansion.
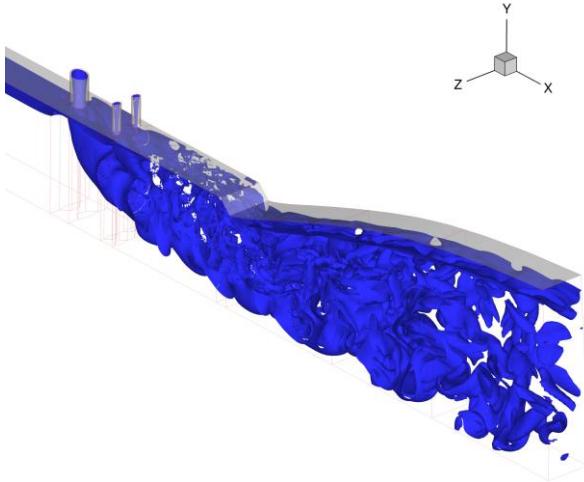
Figure 21. An isosurface of constant total vorticity with a value of $2.0 \cdot 10^5$ (1/s). This simulation used 512 points in the streamwise direction in the grid within the nozzle expansion. Note the continued presence of the vorticity through the nozzle exit.
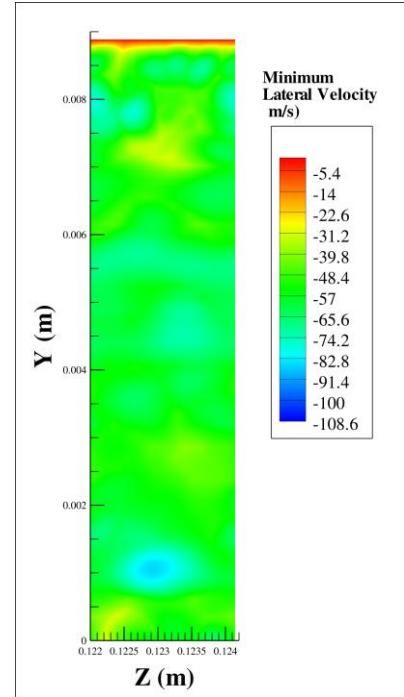


Figure 22. Minimum *W* velocity within the nozzle exit plane for the original grid over the period of the simulation. Note that the minimum is for each *Y, Z* location for all *t*.
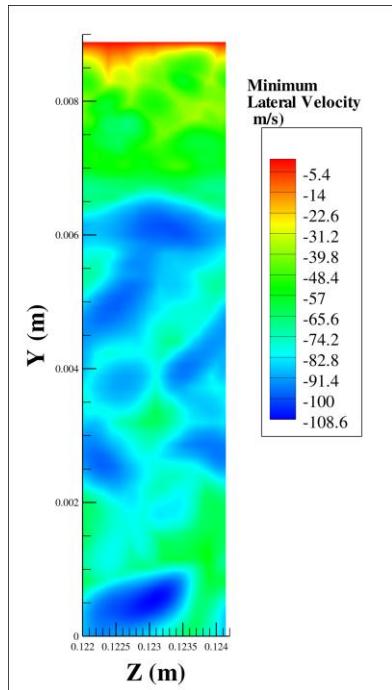


Figure 23. Minimum *W* velocity within the nozzle exit plane for the higher density grid over the period of the simulation. Note that the minimum is for each *Y, Z* location for all *t*.
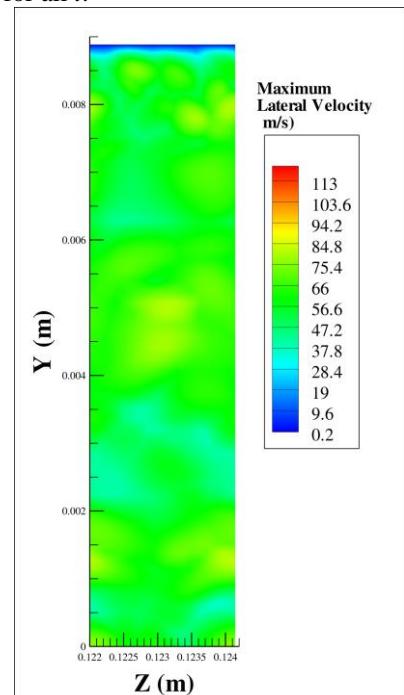


Figure 24. Maximum *W* velocity within the nozzle exit plane for the original grid over the period of the simulation. Note that the minimum is for each *Y, Z* location for all *t*.
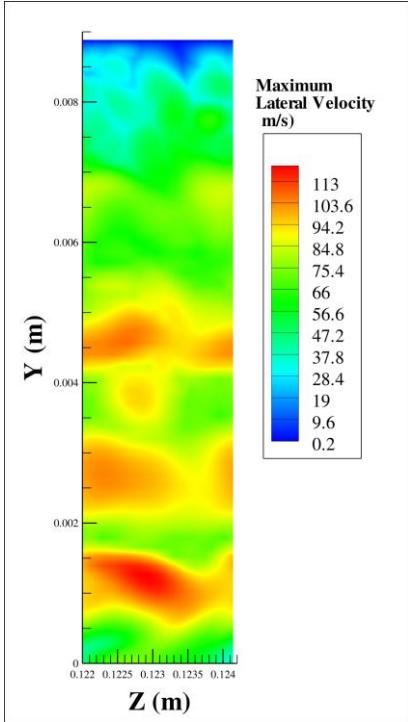
Figure 25.  Maximum *W* velocity within the nozzle exit plane for the higher density grid over the period of the simulation.  Note that the minimum is for each *Y, Z* location for all *t*.
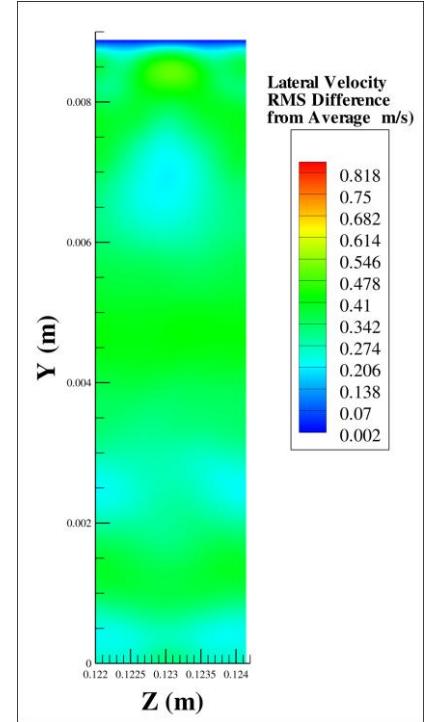


Figure 26.  RMS *W* velocity difference from the average value within the nozzle exit plane for the original grid over the period of the simulation.
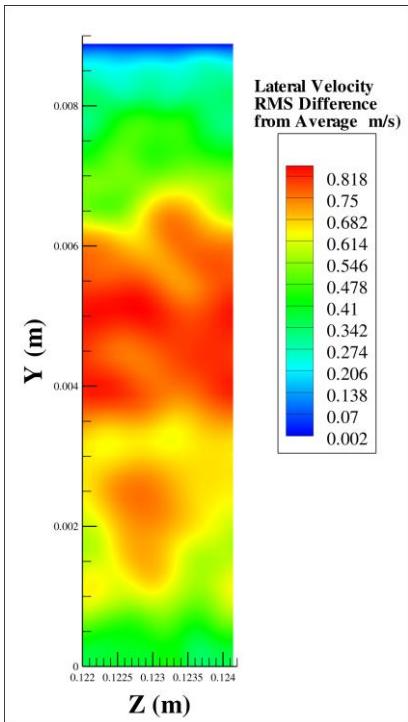


Figure 27.  RMS *W* velocity difference from the average value within the nozzle exit plane for the higher density grid over the period of the simulation.
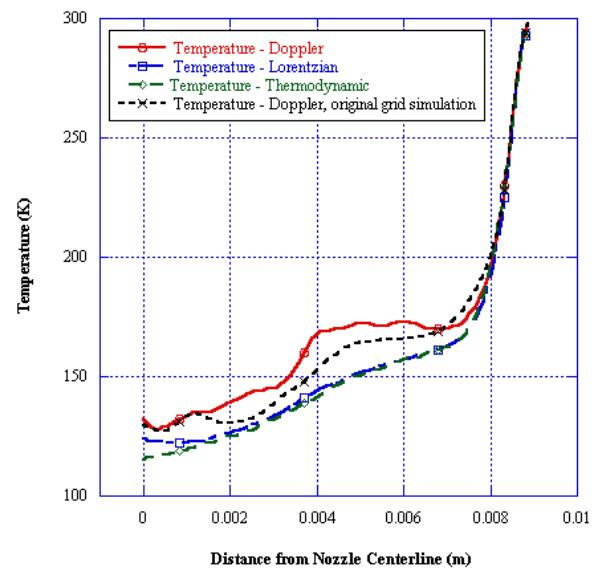


Figure 28.  Comparison of temperature values from the 13 species, 52 reaction simulation for both the original and high density grid simulations.  Note that the Dopper temperature is somewhat higher with the high density grid simulation.

17
American Institute of Aeronautics and Astronautics
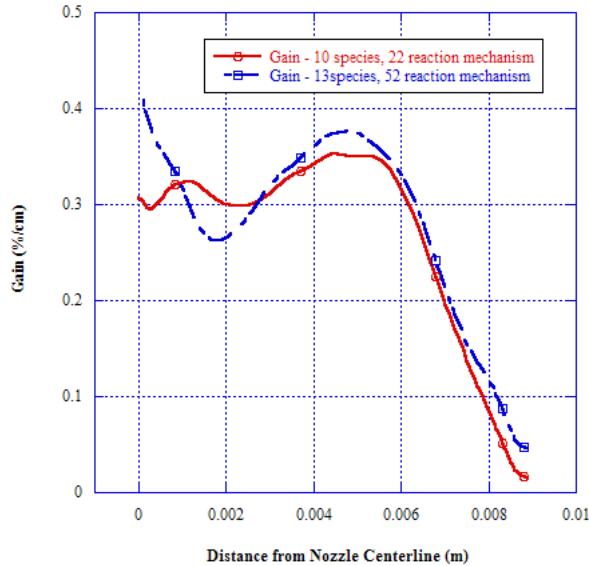
Figure 29.  Comparison of the linecenter gain values versus Y coordinate (distance from the centerline) between the 10 species, 22 reaction and the 13 species, 52 reaction COIL chemistry model simulations.
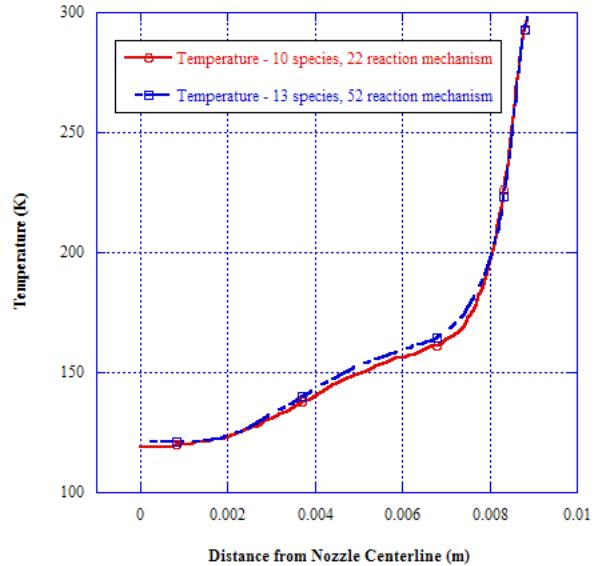


Figure 30.  Comparison of the average temperature values versus Y coordinate (distance from the centerline) between the 10 species, 22 reaction and the 13 species, 52 reaction COIL chemistry model simulations.